

Nonreciprocal magnetoacoustic waves in synthetic antiferromagnets with Dzyaloshinskii–Moriya interaction

M. Küß,^{1,*} M. Hassan,² Y. Kunz,³ A. Hörner,¹ M. Weiler,³ and M. Albrecht²

¹*Experimental Physics I, Institute of Physics, University of Augsburg, 86135 Augsburg, Germany*

²*Experimental Physics IV, Institute of Physics, University of Augsburg, 86135 Augsburg, Germany*

³*Fachbereich Physik and Landesforschungszentrum OPTIMAS,*

Technische Universität Kaiserslautern, 67663 Kaiserslautern, Germany

(Dated: December 23, 2022)

The interaction between surface acoustic waves (SAWs) and spin waves (SWs) in a piezoelectric/magnetic thin film heterostructure yields potential for the realization of novel microwave devices and applications in magnonics. In the present work, we investigate the SAW-SW interaction in a Pt/Co(2)/Ru(0.85)/Co(4)/Pt synthetic antiferromagnet (SAF) composed of two ferromagnetic layers with different thicknesses separated by a thin nonmagnetic Ru spacer layer. Because of the combined presence of interfacial Dzyaloshinskii–Moriya interaction (iDMI) and interlayer dipolar coupling fields, the optical SW mode shows a large nondegenerate dispersion relation for oppositely propagating SWs. Due to SAW-SW interaction, we observe nonreciprocal SAW transmission in the piezoelectric/SAF hybrid device. The equilibrium magnetization directions of both Co layers are manipulated by an external magnetic field to set a ferromagnetic, canted, or antiferromagnetic configuration. This has a strong impact on the SW dispersion, its nonreciprocity, and SAW-SW interaction. The experimental results are in agreement with a phenomenological SAW-SW interaction model, which considers the interlayer exchange coupling, iDMI, and interlayer dipolar coupling fields of the SWs.

I. INTRODUCTION

Surface acoustic waves (SAWs) are widely employed in research and technology nowadays. Efficient excitation and detection of SAWs is possible with metallic grating structures - so-called interdigital transducer structures (IDTs) - on piezoelectric crystals [1]. These acoustic devices are employed in telecommunications as rf-filters [2, 3] and have further applications, e.g., in microfluidic lab-on-a-chip devices [4, 5], quantum acoustics [6, 7], and sensors [8–10]. In general, SAWs show large propagation lengths but are generally reciprocal and offer little control parameters.

In contrast, spin waves (SWs) in magnetic media have low propagation lengths but can be controlled in many ways [11]. For instance, the dispersion $f(k)$ of SWs can be reprogrammed by external magnetic fields or electrical currents [12, 13]. Furthermore, $f(k)$ can show different resonance frequencies for counter-propagating SWs with wave vectors k^+ and k^- , as depicted in Fig. 1(a). This frequency nonreciprocity $\Delta f_{\pm} = f(k^+) - f(k^-)$ can be pronounced in heavy metal/ferromagnetic films due to the interfacial Dzyaloshinskii–Moriya interaction (iDMI) [14–18] and in magnetic bi- and multilayers with nonmagnetic spacer layers via the interlayer dipolar coupling (IDC) fields of the SWs [12, 19, 20]. The physical origin of the nonreciprocity lies in the opposite chiralities of counter-propagating SWs. The energy degeneracy is lifted due to chirality-dependent interactions such as iDMI or dipolar interactions. The nonmagnetic

spacer layer in magnetic bilayers can give rise to Ruderman–Kittel–Kasuya–Yosida (RKKY)-type [21] indirect interlayer exchange coupling, which can result in a preferred antiferromagnetic alignment of the equilibrium magnetizations of both ferromagnetic layers. For simplicity, we refer to these layers as synthetic antiferromagnets (SAFs) [22]. The nonreciprocity Δf_{\pm} in such SAF layers can be especially strong, reconfigurable, and tuneable by the composition of the materials [12]. It was recently predicted that the nonreciprocity in SAFs can be even further enhanced by the additional presence of iDMI [23].

The advantageous properties of SAWs and SWs can be combined in piezoelectric-ferromagnetic hybrid structures [24], as shown in Fig. 1(b). Phonon-magnon coupling is mediated by, e.g., magnetoelastic interaction and opens up the route toward energy-efficient SW excitation and manipulation in the field of magnonics [25]. But also the properties of the SAW are greatly affected by resonant magnetoacoustic interaction. It was recently demonstrated that resonant magnetoacoustic coupling between SAWs and nonreciprocal SWs can give rise to large nonreciprocal SAW transmission, which may be useful for new devices such as microwave acoustic isolators or circulators [26–30]. Hereby, the nonreciprocity of SWs is caused by either iDMI [26, 31, 32] or IDC in magnetic bilayers with [27–29, 33] and without [30] interlayer exchange coupling through nonmagnetic spacer layers.

Here, we experimentally study the impact of a large nonreciprocal SW dispersion Δf_{\pm} of a SAF with iDMI and IDC on the SAW transmission in a piezoelectric/magnetic heterostructure, as shown in Fig. 1. The nonreciprocity Δf_{\pm} of the low-frequency optical SW

* matthias.kuess@physik.uni-augsburg.de.

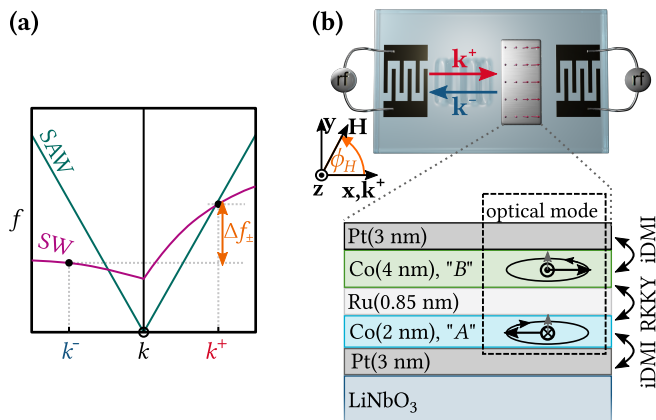


FIG. 1. (a) Interlayer dipolar coupling and iDMI can give rise to a very high nonreciprocity $\Delta f_{\pm} = f(k^+) - f(k^-)$ of the SW dispersion in a synthetic antiferromagnet (SAF) with iDMI. Thus, the SAW-SW resonance differs for counter-propagating SAWs. (b) Illustration of the investigated magnetoacoustic hybrid device and the coordinate system used. The nonreciprocity of the magnetoacoustically excited SWs in the Pt/Co(2)/Ru/Co(4)/Pt SAF is characterized by different transmission magnitudes of oppositely propagating waves \mathbf{k}^+ and \mathbf{k}^- . For moderate excitation frequencies ($f < 7$ GHz) solely the optical mode can be excited in the antiferromagnetic (AFM) configuration. This is schematically shown by the trajectory of the precessing magnetic moments (black arrows) in the Damon-Eshbach geometry ($\phi_0^l = \pm 90^\circ$).

mode is enhanced by the individual additive nonreciprocal contributions of iDMI and IDC in the investigated Pt/Co(2)/Ru(0.85)/Co(4)/Pt SAF thin film sample (all thicknesses are given in nm). Moreover, the equilibrium magnetization directions of both magnetic Co layers are tuned by an external magnetic field to a ferromagnetic, canted, and antiferromagnetic configuration. We demonstrate that these configurations govern the SW resonance frequency, magnetoacoustic driving fields, and SAW transmission. The experimental results are well reproduced for multiple excitation frequencies by an extended phenomenological model, which considers the interlayer exchange coupling, IDC fields of the SWs, and iDMI.

II. THEORY

We describe the SAW-SW interaction in SAFs consisting of a bottom magnetic layer *A* (2 nm Co), a non-magnetic spacer layer, and a top magnetic layer *B* (4 nm Co), with a phenomenological model. The thicknesses and saturation magnetizations of the magnetic layers are d^l and M_s^l , respectively, with $l = A, B$. As depicted in Figs. 1(b) and 2(b), the *x* axis of the *xyz* coordinate system is parallel to the SAW propagation direction k^+ and the *z* axis is normal to the plane of the magnetic film. The wave vectors k of SAW and SW are defined as $\mathbf{k} = k\hat{\mathbf{x}}$. For counter-propagating waves with wave vectors $|k|$, we

write k^+ ($k > 0$) and k^- ($k < 0$). In contrast to previous studies on magnetoacoustic interaction in magnetic bilayers [27, 29, 30], we consider SAFs with iDMI, IDC, and bilinear interlayer exchange coupling (IEC). The combination of all these interaction mechanisms gives rise to different configurations of the equilibrium magnetization and a large nonreciprocity Δf_{\pm} of the SW dispersion.

A. Equilibrium state of the magnetization

First, we calculate the equilibrium orientations ϕ_0^l of the magnetizations \mathbf{M}^l in the *xyz* coordinate system by numeric local energy minimization utilizing a macrospin model [23, 34–37]. For both layers, we take into account the Zeeman energy with the external magnetic field magnitude H and direction ϕ_H and phenomenological in-plane uniaxial anisotropies with the magnitudes H_{ani}^l and the directions ϕ_{ani}^l with respect to the *x* axis. Thin film shape anisotropy fields are partly compensated by surface anisotropy fields $H_k\hat{\mathbf{z}}$. The equilibrium magnetizations are aligned in the *xy* plane ($M_z^l = 0$). The bilinear interlayer exchange coupling with the effective interlayer coupling constant J_{eff} favors an antiparallel alignment ($J_{\text{eff}} < 0$) of \mathbf{M}^A and \mathbf{M}^B . We use Eq. (A1) of Appendix A to calculate ϕ_0^l .

The calculated equilibrium magnetization orientations $\phi_0^l(\mu_0 H)$ and resulting M - H magnetization hysteresis loop of the sample are shown in Figs. 2(a) and 3(c) as a function of the external magnetic field magnitude $\mu_0 H$. The parameters used are listed in Table I. The magnetization configuration shows three different magnetic states - namely the ferromagnetic (FM, $\phi_0^A = \phi_0^B$), the canted (C, $\phi_0^A \neq \{\phi_0^B, \phi_0^B \pm 180^\circ\}$), and the antiferromagnetic (AFM, $\phi_0^A = \phi_0^B \pm 180^\circ$) configuration. While the FM configuration is favored by the Zeeman energy at high fields $|\mu_0 H| \gtrsim 460$ mT, the AFM configuration is mediated by the antiferromagnetic interlayer exchange coupling at low fields $|\mu_0 H| \lesssim 150$ mT. The three different magnetization configurations are also experimentally observed in the M - H magnetometry measurements in Fig. 2(a), which were obtained with the external magnetic field aligned in the plane of a reference sample SAF along $\phi_H = 0^\circ$. More details about the experimental results will be given later. The equilibrium magnetization orientations have a strong impact on the SW dispersion and the magnetoacoustic driving fields, as will be discussed next.

B. Spin wave dispersion

The dispersion of a SAW $\omega = c_{\text{SAW}}|k|$ in a homogeneous substrate with the angular frequency $\omega = 2\pi f$ is defined by a constant propagation velocity of about $c_{\text{SAW}} \approx 3500$ m/s [3], as schematically depicted in Fig. 1(a). In contrast, the dispersion of SWs in SAFs

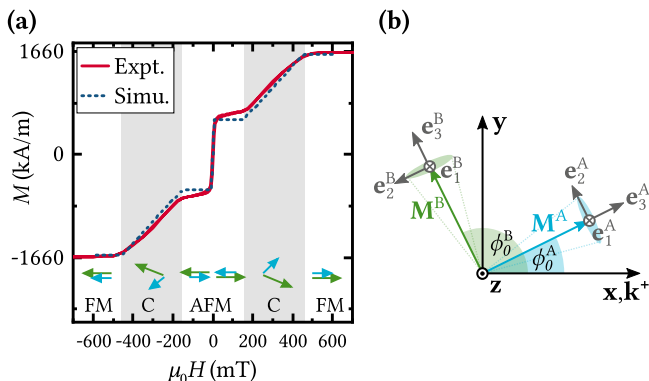


FIG. 2. (a) The M - H hysteresis loop of the Pt/Co(2)/Ru/Co(4)/Pt SAF with the magnetic field applied in the xy easy magnetization plane along $\phi_H = 0^\circ$. The magnetization hysteresis loops of experiment and simulation agree well. Both show a FM, C, and AFM configuration, which are additionally schematically depicted by the blue (layer A) and green (layer B) magnetization vectors. The parameters of the simulation are given in Table I and $\phi_H = 0^\circ$ is assumed. (b) The magnetization dynamics and the effective magnetoacoustic driving fields are described in individual $(\mathbf{e}_1^l, \mathbf{e}_2^l, \mathbf{e}_3^l)$ -coordinate systems of both layers. Here, the \mathbf{e}_3^l -axes are defined by the equilibrium orientations ϕ_0^l of the magnetizations \mathbf{M}^l .

depends on multiple material parameters and its behavior is more complicated.

To calculate the SW dispersion, we follow the approach of Ref. [30] and solve the coupled linearized Landau–Lifshitz–Gilbert (LLG) equations of both magnetic layers. To this end, we employ the $(\mathbf{e}_1^l, \mathbf{e}_2^l, \mathbf{e}_3^l)$ coordinate systems, shown in Fig. 2(b). Hereby, the \mathbf{e}_3^l -directions correspond to the equilibrium magnetization orientations, the \mathbf{e}_2^l -directions are aligned in the plane of the magnetic film, and the \mathbf{e}_1^l -directions are parallel to the film normal. The magnetization precession is defined by the transverse magnetization components $M_{1,2}^l = M_s^l m_{1,2}^l$ and is assumed to be small ($M_{1,2}^l \ll M_s^l$).

We formulate the effective fields of the LLG equations in the $(\mathbf{e}_1^l, \mathbf{e}_2^l, \mathbf{e}_3^l)$ coordinate systems as

$$\mathbf{H}_{\text{eff},123}^l = \mathbf{H}_{\text{eff},123,\text{intra}}^l + \mathbf{H}_{\text{eff},123,\text{IEC}}^l + \mathbf{H}_{\text{eff},123,\text{IDC}}^l + \begin{pmatrix} h_1^l \\ h_2^l \\ 0 \end{pmatrix}. \quad (1)$$

with the intralayer effective fields $\mathbf{H}_{\text{eff},123,\text{intra}}^l$ [31] caused by the (i) Zeeman energy, (ii) in-plane uniaxial magnetic anisotropy, (iii) out-of-plane surface anisotropy, (iv) intralayer exchange interaction, (v) intralayer dipolar fields, and (vi) iDMI fields $\mathbf{H}_{\text{eff},123,\text{DMI}}^l$. The interlayer coupling is mediated by bilinear exchange fields $\mathbf{H}_{\text{eff},123,\text{IEC}}^A$ and the dipolar fields $\mathbf{H}_{\text{eff},123,\text{IDC}}^l$ of the SWs. The terms for $\mathbf{H}_{\text{eff},123,\text{DMI}}^l$, $\mathbf{H}_{\text{eff},123,\text{IEC}}^l$ and $\mathbf{H}_{\text{eff},123,\text{IDC}}^l$ are taken from Refs. [12, 14], rewritten in the $(\mathbf{e}_1^l, \mathbf{e}_2^l, \mathbf{e}_3^l)$ coordinate systems, and given in Eqs. (B1)–(B3) in Appendix B. Moreover, the SAW-SW interaction is me-

diated by small time-varying magnetoacoustic driving fields $h_{1,2}^l$, as defined in the next section. From the LLG equations, we calculate the 4×4 magnetic susceptibility tensor which describes the magnetic response

$$\begin{pmatrix} M_1^A \\ M_2^A \\ M_1^B \\ M_2^B \end{pmatrix} = \bar{\chi} \begin{pmatrix} h_1^A \\ h_2^A \\ h_1^B \\ h_2^B \end{pmatrix}. \quad (2)$$

to $h_{1,2}^l$. The SW resonance frequency $f(\mu_0 H)$ is obtained by setting $\det(\bar{\chi}^{-1}) = 0$ and taking the real part of the solution. The linewidth Δf_{HWHM} is given by the corresponding imaginary part. Here, we neglect mutual spin pumping between both magnetic layers of the SAF [38, 39].

As an example, we calculate the SW resonance $f(\mu_0 H)$ of our Pt/Co/Ru/Co/Pt sample in Fig. 3(a). The assumed parameters are summarized in Table I, $\phi_H = 45^\circ$ is the external magnetic field direction and $|k^\pm| = 13.1 \mu\text{m}^{-1}$ is the wave vector of a SAW with a frequency of 6.77 GHz. Only the low-frequency SW mode, which we refer to the SW optical mode [23], is shown. The resonance frequency of the high-frequency SW acoustic mode is much higher ($f > 20$ GHz) than the SAW excitation frequency (6.77 GHz) because of the antiferromagnetic interlayer exchange coupling. Local minima in the SW resonance frequency appear where the static magnetization configuration (FM, C, AFM) transforms into another one.

In addition, counter-propagating SWs with wave vectors k^+ and k^- have shifted resonance frequencies. The origin of the large frequency nonreciprocity $\Delta f_\pm = f(k^+) - f(k^-)$ is characterized in Fig. 3(b) in more detail. Since iDMI and IDC are well-known to cause frequency nonreciprocity, the impact of both individual contributions on Δf_\pm is calculated by setting the corresponding other effective field $\mathbf{H}_{\text{eff},123,\text{IDC}}^l$ or $\mathbf{H}_{\text{eff},123,\text{iDMI}}^l$ to zero. A constructive superposition of Δf_\pm caused by iDMI and IDC results in a very large frequency nonreciprocity of more than 2 GHz in the AFM configuration at $\phi_H = 45^\circ$. The impact of iDMI of the top and bottom ferromagnetic layer on Δf_\pm is expected to have additive contributions in the AFM configuration [23]. The nonreciprocity Δf_\pm is low in the FM configuration in comparison to the AFM configuration. Furthermore, the sign of Δf_\pm switches between the AFM and FM configuration. A more detailed theoretical discussion about the enhancement of Δf_\pm in different antiferromagnetically coupled magnetic bilayers with iDMI and IDC was recently presented by A. Franco and P. Landeros [23]. The Pt/Co(2)/Ru(0.85)/Co(4)/Pt SAF of our study shows a similar behavior as the considered Pt/Co(1.5)/Cu(0.95)/Co(2)/Pt SAF in their work [23].

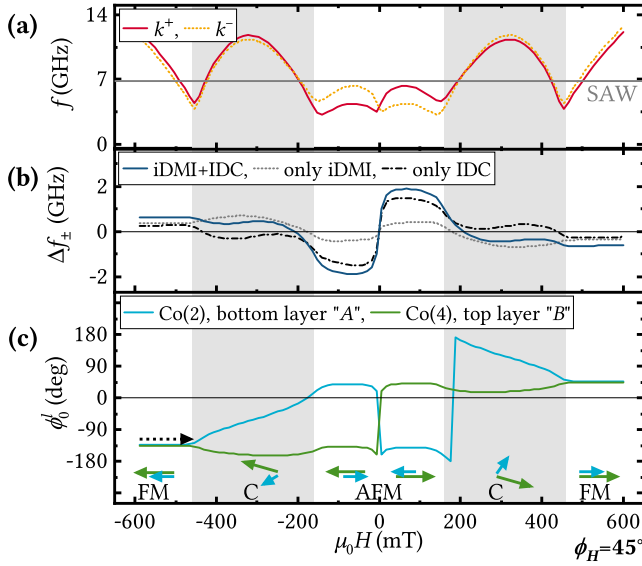


FIG. 3. (a) The calculated resonance frequency of the optical SW mode as a function of the external magnetic field $\mu_0 H$ shows nondegenerated frequencies for counter-propagating SWs with wave vectors k^+ and k^- . Calculated for $\phi_H = 45^\circ$ and $|k^\pm| = 13.1 \mu\text{m}^{-1}$. (b) The large frequency nonreciprocity $\Delta f_\pm = f(k^+) - f(k^-)$ can be understood as an additive interplay of both individual contributions of iDMI and IDC [23]. (c) The equilibrium orientations ϕ_0^l of the magnetizations \mathbf{M}^l , which are schematically depicted by the arrows govern the nonreciprocal SW resonance.

C. Magnetoacoustic driving fields

The propagating SAW causes strain ε_{ij} and lattice rotation ω_{ij} in the SAF with $i, j = x, y, z$. Via SAW-SW coupling mechanisms, such as inverse magnetostriction, the SAW modulates the magnetic free energy. The corresponding effective magnetoacoustic driving field as a function of SAW power P_{SAW} in the $(\mathbf{e}_1^l, \mathbf{e}_2^l)$ plane can be written [31] as

$$\begin{pmatrix} h_1^l \\ h_2^l \end{pmatrix} = \begin{pmatrix} \tilde{h}_1^l \\ \tilde{h}_2^l \end{pmatrix} \sqrt{\frac{k^2}{R\omega W}} \sqrt{P_{\text{SAW}}(x)} e^{i(kx - \omega t)}. \quad (3)$$

Here, W is the width of the aperture of the IDT and R is a constant [40]. The normalized effective magnetoelastic driving fields \tilde{h}_1^l and \tilde{h}_2^l of a Rayleigh wave with strain components $\varepsilon_{ij=xx, xz} \neq 0$ are [31, 41]

$$\begin{pmatrix} \tilde{h}_1^l \\ \tilde{h}_2^l \end{pmatrix} = \frac{2}{\mu_0} \left[b_1^l \tilde{a}_{xx} \begin{pmatrix} 0 \\ \sin \phi_0^l \cos \phi_0^l \end{pmatrix} + b_2^l \tilde{a}_{xz} \begin{pmatrix} \cos \phi_0^l \\ 0 \end{pmatrix} \right], \quad (4)$$

where $b_{1,2}^l$ are the magnetoelastic coupling constants for cubic symmetry of the ferromagnetic layers [41, 42], $\tilde{a}_{ij} = \varepsilon_{ij,0}/(|k||u_{z,0}|)$ are the normalized amplitudes of the strain, and $\varepsilon_{ij,0}$ are the complex amplitudes of the strain. Furthermore, $u_{z,0}$ is the amplitude of the lattice displacement in the z direction. Because the wavelength

$\lambda = (2\pi)/|k|$ of the SAW ($\lambda \gtrsim 500 \text{ nm}$) is much larger than the film thickness of the SAF ($\approx 10 \text{ nm}$) we assume constant strain in z direction. For the sake of simplicity, we neglect non-magnetoelastic interactions, like magneto-rotation coupling [31, 32, 43], spin-rotation coupling [44–46], and gyromagnetic coupling [47].

The magnetoacoustic driving fields result in a torque on the equilibrium magnetizations of both individual magnetic layers. Whether these torques add up or cancel for the excitation of SWs in SAFs depends on the directions of the magnetoacoustic driving fields and on the SW modes which can potentially be excited in the different magnetization configurations (FM, C, AFM). To demonstrate the impact of the magnetoacoustic driving fields on the excited SW modes, we calculated from the magnetization equilibrium directions ϕ_0^l the magnitude of h_2^l of a purely longitudinal strain wave with $\varepsilon_{xx} \neq 0$ for external magnetic field sweeps from -600 mT to 600 mT at multiple angles $|\phi_H| \leq 90^\circ$. The results are shown in Figs. 4(a) and 4(b).

For the FM and AFM configuration, the magnetoelastic driving field $|h_2^l|$ of both magnetic layers follows the well-known four-fold symmetry [48] with maxima at $\phi_H = \pm 45^\circ$ and minima at $\phi_H = 0^\circ, \pm 90^\circ$. For the C configuration, the symmetry of $|h_2^l|$ is more complicated because the equilibrium magnetization is not parallel or antiparallel to the external magnetic field. Note that the direction of h_2^l in the fixed xyz coordinate system depends on the direction of the \mathbf{e}_2^l -axes [see Fig. 2(b)].

In Figs. 4(c)–4(e) we show an illustration of the driving fields h_2^l and the SW modes, which can potentially be excited in the FM, C, and AFM configuration of the investigated Pt/Co/Ru/Co/Pt SAF for $\phi_H = 45^\circ$. The optical SW mode in the FM configuration is described by an anti-phase magnetization precession [23]. In contrast, the magnetization precession of the optical SW mode in the AFM configuration is in-phase in the \mathbf{e}_1^l direction and anti-phase in the \mathbf{e}_2^l direction [27]. The drawing of the C configuration depicts only one possible situation and is in general more complicated, since the SW mode and driving field change with the external magnetic field magnitude. Together with the right-handed magnetization-precession, the magnetoelastic excitation of SWs in the AFM configuration is efficient, whereas it is not efficient in the FM and depicted C configuration.

D. Absorbed power

The total absorbed power P_{abs} of the SAW, caused by SAW-SW interaction, is the sum of the absorbed power

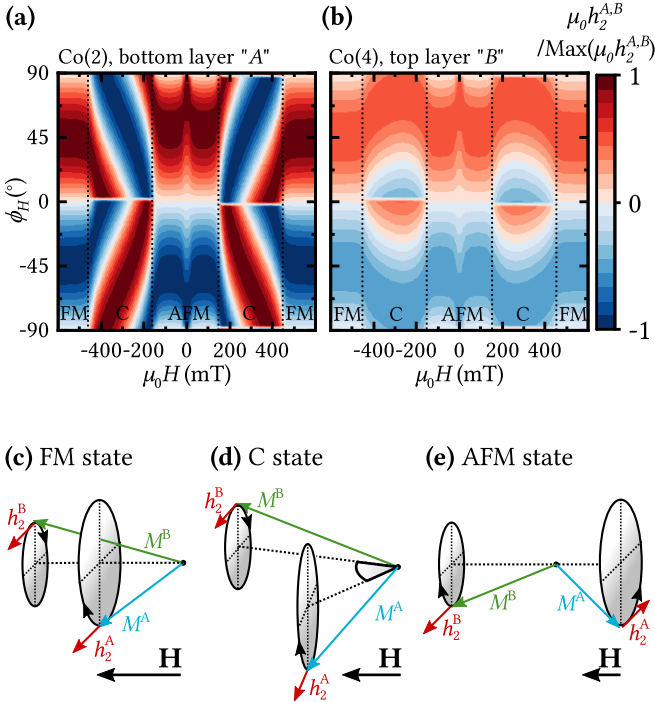


FIG. 4. Magnetoacoustic driving field and impact on the excited SW modes in the investigated SAF sample. (a),(b) The dominating in-plane component h_2^l of the effective magnetoacoustic driving field of a Rayleigh-type SAW in the individual magnetic layers of the SAF is calculated with Eq. (4) on basis of the equilibrium magnetization directions ϕ_0^l and the parameters in Table I. The symmetry of $|h_2^l|$ follows the well-known four-fold symmetry [48] in the FM and AFM configuration, but is more complicated in the C configuration. (c)–(e) Schematic drawings of the excited optical SW modes and driving fields h_2^l , which can potentially be excited in the FM, C, and AFM configuration for $\phi_H = 45^\circ$. Here, the acoustic SW modes cannot be magnetoacoustically excited since its resonance frequency is much higher ($f > 20$ GHz) than the SAW excitation frequency (6.77 GHz). While the magnetoelastic excitation of SWs in the AFM configuration is efficient, it is not efficient in the FM configuration. The drawing of the C configuration depicts only one possible situation. The direction of h_2^l is defined by the direction of the e_2 axes (see Fig. 2).

of the individual layers. Following Ref. [30], we write

$$P_{\text{abs}} = P_0 \left(1 - \exp \left\{ -\tilde{C} \operatorname{Im} \left[\left(\begin{array}{c} d^A \tilde{h}_1^A \\ d^A \tilde{h}_2^A \\ d^B \tilde{h}_1^B \\ d^B \tilde{h}_2^B \end{array} \right)^* \tilde{\chi} \left(\begin{array}{c} \tilde{h}_1^A \\ \tilde{h}_2^A \\ \tilde{h}_1^B \\ \tilde{h}_2^B \end{array} \right) \right] \right\} \right)$$

with $\tilde{C} = \frac{1}{2} \mu_0 l_f \left(\frac{k^2}{R} \right)$, (5)

where l_f is the length of the magnetic thin film along the x axis. Finally, to directly simulate the experimentally determined relative change of the SAW transmission

ΔS_{ij} on the logarithmic scale, we use

$$\Delta S_{ij} = 10 \log \left(\frac{P_0 - P_{\text{abs}}}{P_0} \right) \quad \text{with } ij = \begin{cases} 21, & \text{for } k^+ \\ 12, & \text{for } k^- \end{cases} \quad (6)$$

for SAWs propagating parallel (k^+) and antiparallel (k^-) to the x axis.

III. EXPERIMENTAL SETUP

We used magnetron sputter deposition for the preparation of the Pt(3)/Co(2)/Ru(0.85)/Co(4)/Pt(3)/Si₃N₄(3) SAF on a piezoelectric Y-cut Z-propagation LiNbO₃ substrate. The deposition parameters are detailed in Appendix C. In such multilayers made out of Co/Ru(d_s)/Co especially strong antiferromagnetic interlayer exchange coupling has been observed for $0.5 \text{ nm} \lesssim d_s \lesssim 1 \text{ nm}$ [34, 49, 50]. Furthermore, the Pt layers are known to induce strong iDMI in Co [18, 51, 52]. To obtain a large nonreciprocity Δf_{\pm} of the optical SW mode by a combined action of iDMI and IDC, we follow the design rules of Ref. [23]. The bottom Co(2)-layer has a lower natural frequency and a larger thickness-averaged effective DMI constant D_{eff}^A than the top Co(4)-layer because of its lower film thickness and lower effective magnetization $M_{\text{eff}}^l = M_s^l - H_k^l$. Therefore, the Co(2)-layer governs the low frequency optical SW mode of the SAF which should be strongly affected by the relatively large D_{eff}^A .

The SAW transmission measurements are carried out with two single finger IDTs that are made out of Ti(5)/Al(70), have three finger pairs with a periodicity of $1.7 \mu\text{m}$, and can be operated at multiple higher harmonic resonance frequencies of up to ~ 7 GHz. The Y-cut Z-propagation LiNbO₃ substrate gives rise to Rayleigh-type SAW excitation [3]. More details about the IDT geometry are given in the Supplemental Material of Ref. [31].

The M - H hysteresis loop of the prepared SAF was measured by superconducting quantum interference device-vibrating sample magnetometry (SQUID-VSM) and is presented in Fig. 2(a). The SAF shows the expected behavior with FM, C, and AFM magnetization configurations.

On additionally prepared Pt(3)/Co(2)/Ru(0.85)/Si₃N₄(3) and Ru(0.85)/Co(4)/Pt(3)/Si₃N₄(3) single reference samples SQUID-VSM magnetometry and broadband ferromagnetic-resonance (bbFMR) measurements were carried out to further characterize the magnetic properties of the individual Co layers.

The SAW transmission of our delay line device was measured by a vector network analyzer. Based on the low propagation velocity of the SAW, a time-domain gating technique was employed to exclude spurious signals [53], in particular, electromagnetic crosstalk. We use the relative change of the background-corrected SAW transmission signal

$$\Delta S_{ij}(\mu_0 H) = S_{ij}(\mu_0 H) - S_{ij}(600 \text{ mT}) \quad (7)$$

to characterize SAW-SW coupling. Here, ΔS_{ij} is the magnitude of the complex transmission signal with $ij = 21, 12$. In all measurements, the magnetic field is swept from -600 mT to 600 mT corresponding to full magnetic saturation.

IV. DISCUSSION

A. Frequency dependence

In Figs. 5(a)–5(d), we show the magnetoacoustic transmission ΔS_{21} of the prepared Pt/Co/Ru/Co/Pt SAF as a function of external magnetic field magnitude $\mu_0 H$ and orientation ϕ_H . The measurements were carried out for all four harmonic frequencies $f = 1.00, 3.00, 5.03, 6.77$ GHz and corresponding wave vectors $k = 1.9, 5.8, 9.8, 13.1 \mu\text{m}^{-1}$ of the acoustic delay line. The vertical dotted lines indicate the transitions of the static magnetization configurations (FM, C, AFM) according to the M - H hysteresis loop in Fig. 2(a). In comparison to earlier studies performed on magnetic single layers [31, 41, 48, 54], magnetic bilayers with zero inter-layer exchange coupling [30], and symmetric SAFs with $d^A = d^B$ [29, 33], many resonances show up for the asymmetric SAF with $d^A \neq d^B$. The resonances in the FM and AFM configuration are at maximum at $|\phi_H| \approx 45^\circ$. In contrast, the resonances in the C configuration show up at $|\phi_H| \approx 0^\circ, 90^\circ$. Whereas the resonances in the FM and C configuration have a low intensity and relatively narrow linewidth, the intensity and linewidth of the resonances in the AFM configuration are large.

The simulations of $\Delta S_{21}(\mu_0 H, \phi_H)$ are shown in Figs. 5(e)–5(h). Moreover, we simulate the SW resonances f , SW linewidths indicated by $f \pm \Delta f_{\text{HWHM}}$, and SAW excitation frequencies in Figs. 5(i)–5(l) for $\phi_H = 45^\circ$. Note that the SW resonances $f(\mu_0 H)$ are in general not constant, but are a function of ϕ_H . All simulations were carried out with the parameters given in Table I. We took an increase of α^l with decreasing excitation frequency [31] into account, which is modeled by Eq. (D1). More details about the simulation parameters can be found in Appendix D.

The simulation and experiment displayed in Fig. 5 show a rather good quantitative agreement with respect to all salient features such as resonance fields, linewidth, and transmission magnitude in the FM, C, and AFM configuration. Only the simulation of ΔS_{21} at 1 GHz shows about five times too large amplitudes in ΔS_{21} . The magnetoacoustic resonances at 1 GHz in Figs. 5(d) and 5(h) result from highly off-resonant excitation and occur where the static magnetization transforms from AFM to C configuration and around zero field switching. The too-large amplitudes of the simulation might be caused by deviations of the magnetization reversal from the macrospin approach (domain formation, etc.), which could be especially significant where the static configuration (FM, C, AFM) transforms into another one and

around zero field.

In the AFM configuration at $\phi_H > 0$ and $0 < \mu_0 H < 150$ mT, the resonance with high linewidth at 6.77 GHz changes to two resonances at 5.03 GHz, as shown in Figs. 5(a) and 5(b). If f is further decreased, the splitting of these two resonances increases [Figs. 5(c) and 5(d)]. As depicted in Figs. 5(i)–5(l), this behavior can be understood by the characteristic behavior of the SW resonance with a local maximum in the AFM configuration at $|\mu_0 H| \approx 60$ mT and a decrease of the SAW excitation frequency. For excitation frequencies f below ~ 3 GHz and above ~ 7 GHz, the SW and SAW resonance frequencies do not match in the narrow field range available of the AFM configuration. There exists a window of excitation frequencies in which resonant SAW-SW interaction is possible in the AFM configuration of SAFs. The range and position of this window can be modified by changing the properties of the SAF (e.g., d^l , J_{eff} , M_s^l).

In line with Fig. 5(i), resonant magnetoacoustic interaction at 6.77 GHz is possible in the FM configuration at $|\mu_0 H| \approx 500$ mT and in the C configuration at $|\mu_0 H| \approx 420$ mT, 200 mT. The slope of $f(\mu_0 H)$ around the SAW-SW resonance fields and the SW linewidth Δf_{HWHM} results in a narrow linewidth ΔH of the SAW-SW resonances in the FM and C configuration and in a broad resonance in the AFM configuration.

In agreement with the discussion of Fig. 4, the magnetoacoustic SW excitation efficiency is governed by the static magnetization configuration with large, medium, and low efficiency in the AFM, C, and FM configuration, respectively. Moreover, in the AFM configuration, the in-plane magnetoacoustic driving fields \tilde{h}_2^l and ΔS_{21} are at maximum at $\phi_H \approx \pm 45^\circ$. In the C configuration, the symmetry of the magnetoacoustic driving field is complex, because the static magnetization directions ϕ_0^l are not parallel or antiparallel to the external magnetic field direction ϕ_H . The dominating in-plane magnetoacoustic driving fields \tilde{h}_2^l , which are shown in Fig. 4, are for 6.77 GHz at the positions of the SAW-SW resonances $|\mu_0 H| \approx 200, 420$ mT in the C configuration at maximum at $\phi_H \approx 0^\circ, \pm 90^\circ$. Thus, the resonances of the SAW transmission ΔS_{21} in the C configuration in Figs. 5(a) and 5(e) are also at maximum at $\phi_H \approx 0^\circ, \pm 90^\circ$. Note that the parameters of the SAF have a strong influence on the symmetry dependence of ΔS_{ij} in the C configuration.

Furthermore, the nonreciprocity of the SW dispersion causes a broken symmetry $f(+\mu_0 H) \neq f(-\mu_0 H)$ in Figs. 5(i)–5(l). According to the effective fields caused by iDMI and IDC in Eqs. (B1) and (B3), the frequency nonreciprocity Δf_{\pm} decreases with a decrease of the wave vector k and SAW excitation frequency f . Therefore, also the maximum nonreciprocity of the SAW transmission magnitude $\Delta S_{\pm}(\mu_0 H, \phi_H) = |\Delta S_{21}(\mu_0 H, \phi_H) - \Delta S_{12}(\mu_0 H, \phi_H)|$ decreases from ~ 2 dB at 6.77 GHz to ~ 0.4 dB at 3 GHz.

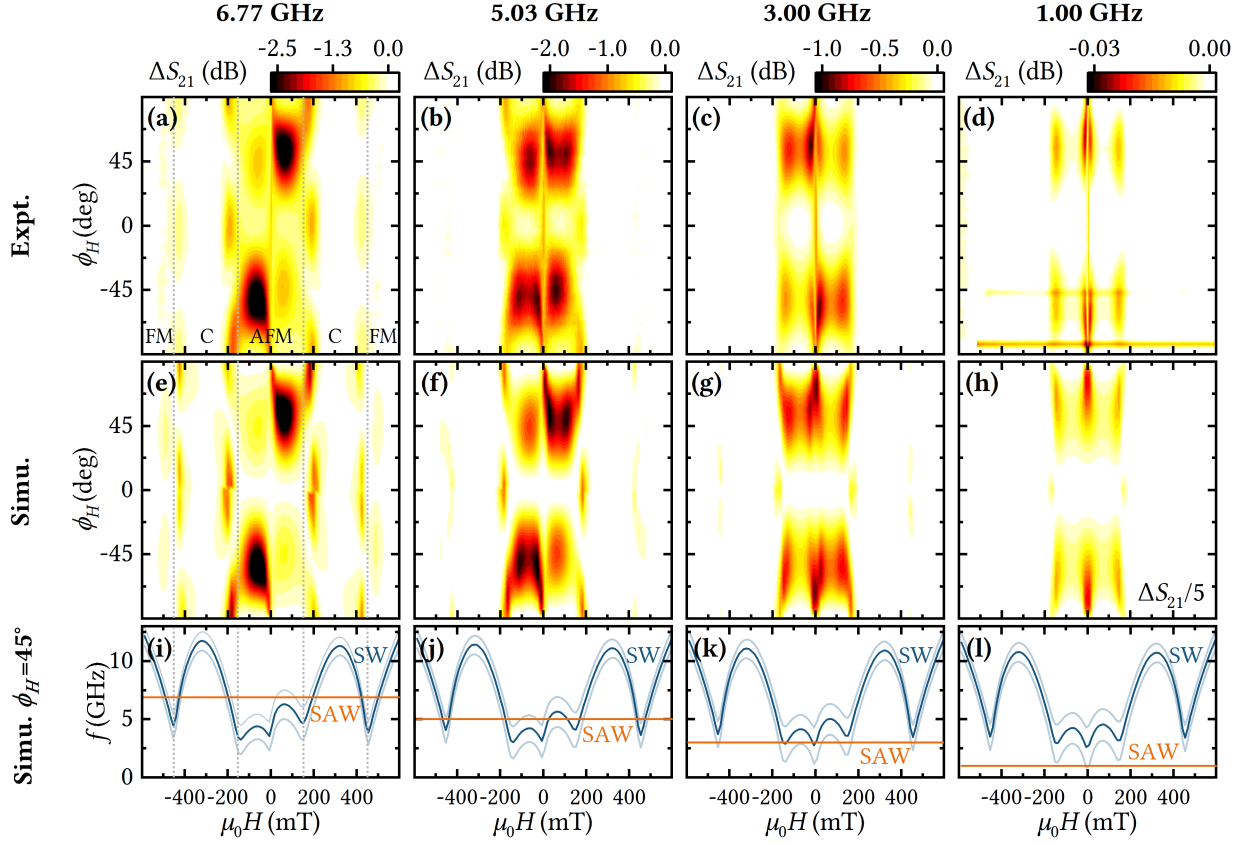


FIG. 5. (a)–(h) The frequency dependence of the magnetoacoustic transmission $\Delta S_{21}(\mu_0 H, \phi_H)$ was determined as a function of external magnetic field magnitude and orientation for all four harmonic resonances of the acoustic delay line. Experiment (Expt.) and simulation (Simu.) show good agreement. (i)–(l) The SW resonances f (blue), SW linewidths indicated by $f \pm \Delta f_{\text{HWHM}}$ (light blue), and SAW excitation frequencies (orange) at $\phi_H = 45^\circ$. Both, simulations (e)–(h) and SW resonances (i)–(l) were calculated with the parameters of Table I and the corresponding wave vector of the SAW ($k_{\text{SW}} = k_{\text{SAW}}$). The nonreciprocity of $\Delta S_{21}(\mu_0 H, \phi_H)$ and of the SW resonance $f(\mu_0 H)$ decrease with decreasing frequency.

TABLE I. Parameters to simulate the equilibrium magnetization directions, SW resonance frequencies, magnetoacoustic driving fields, and the magnetoacoustic transmission ΔS_{21} in Figs. 2–6 at 6.77 GHz. For the simulations at lower frequencies in Fig. 5, the effective SW damping constant α is calculated by Eq. (D1) with the Gilbert damping ($\alpha_{\text{FMR}}^A = 0.031$, $\alpha_{\text{FMR}}^B = 0.019$) and inhomogeneous broadening ($\mu_0 \Delta H_{\text{FMR}}^A = 17$ mT, $\mu_0 \Delta H_{\text{FMR}}^B = 5$ mT) from broadband FMR experiments. For the simulation of ΔS_{12} , the sign of the normalized strain \tilde{a}_{xz} is inverted. Furthermore, the bilinear interlayer exchange coupling constant $J_{\text{eff}} = -0.95$ mJ/m² is extracted from the M - H hysteresis loop and we assume $c_{\text{SAW}} = 3240$ m/s [55] for the SAW propagation velocity in the SAF. More details about the simulation parameters are presented in Appendix D.

	layer l	d^l (nm)	g^l	M_s^l (kA/m)	H_k^l (kA/m)	A_{ex}^l (pJ/m)	D_{eff}^l (mJ/m ²)	$\mu_0 H_{\text{ani}}^l$ (mT)	ϕ_{ani}^l ($^\circ$)	α^l	$b_1^l \tilde{a}_{xx}$ (T)	$b_2^l \tilde{a}_{xz}$ (T)	
	Co(4)	B	4	2.315	1630	667	31 [23, 56]	-0.35	4	0	0.031	1.0	0.22i
	Co(2)	A	2	2.317	1580	1085	31 [23, 56]	+0.70	0	0	0.071	1.9	0.42i

B. Nonreciprocity

After having discussed the frequency dependence, we now look in more detail at the nonreciprocity for the frequency with the largest SAW-SW interaction at $f = 6.77$ GHz. To this end, we show in Fig. 6 the experimental and simulation results of the magnetoacoustic transmission $\Delta S_{21}(\mu_0 H, \phi_H)$ and $\Delta S_{12}(\mu_0 H, \phi_H)$ for counter-

propagating magnetoacoustic waves with the wave vectors k^+ and k^- .

We observe an excellent agreement between experiment and simulation for both, ΔS_{21} and ΔS_{12} . A pronounced nonreciprocity of the transmission ΔS_{\pm} shows only up in the AFM configuration. As discussed next, the reason for the nonreciprocal transmission ΔS_{\pm} lays in the nonreciprocity of the SW dispersion.

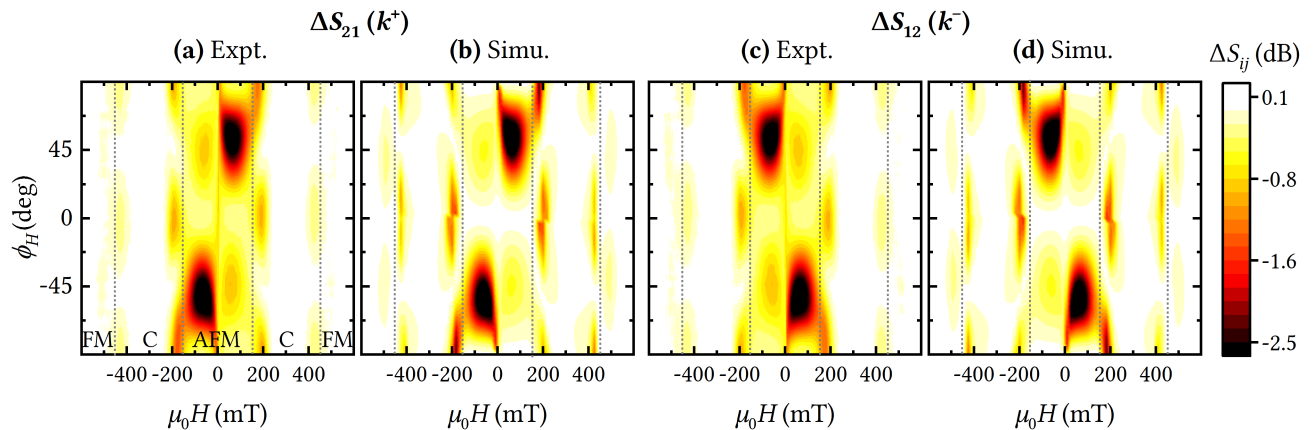


FIG. 6. (a),(c) Change of the SAW transmission $\Delta S_{ij}(\mu_0H, \phi_H)$ for counter-propagating magnetoacoustic waves with the wave vectors k^+ and k^- at 6.77 GHz. The large frequency nonreciprocity Δf_{\pm} of about 2 GHz at $\phi_H = \pm 45^\circ$ in the AFM configuration (see Fig. 3) results in a pronounced nonreciprocity of the SAW transmission. (a),(c) Experiment (Expt.) and (b),(d) corresponding simulations (Simu.) show good overall agreement.

The large frequency nonreciprocity Δf_{\pm} of the SW resonance in Fig. 3(b) is caused by the individual additive contributions of nonreciprocity mediated by iDMI and IDC. Thus, in the AFM configuration for $\mu_0H > 0$ and $\phi_H > 0$, resonant magnetoacoustic interaction is only possible for the SWs with k^+ and the change of the SAW transmission ΔS_{21} presented in Fig. 6 is large. For counter-propagating SAWs (k^-), the transmission $\Delta S_{12}(\mu_0H > 0, \phi_H > 0)$ shows a maximum with very low amplitude. We attribute this maximum to off-resonant magnetoacoustic interaction which is possible because of the large linewidth Δf_{HWHM} of the SW resonance [see Fig. 5(i)]. Besides Gilbert damping, the large effective SW damping α^l results from a large inhomogeneous line broadening and the spin pumping effect [31, 57]. These two effects are very relevant due to the low thicknesses d^l and the Ru- and Pt-interfaces of the magnetic layers. While frequency nonreciprocity is very large with $\Delta f_{\pm} \approx 3$ GHz for the Damon-Eshbach geometry ($\phi_0^l = \pm 90^\circ$), the maximum nonreciprocity of the SAW transmission magnitude is only moderate with $\Delta S_{\pm} \approx 2$ dB. This is again attributed to the large effective SW damping α^l .

In addition to the considered in-plane magnetoacoustic driving fields \tilde{h}_2^l , there are the smaller ($b_2^B \tilde{a}_{xz} < b_1^l \tilde{a}_{xx}$) out-of-plane magnetoacoustic driving fields \tilde{h}_1^l [see Eq. (4)], which could cause nonreciprocal transmission because of a helicity mismatch between the driving fields and magnetizations precession [30, 31, 41, 58]. Since \tilde{h}_1^A and \tilde{h}_1^B are parallel (antiparallel) in the FM configuration (AFM configuration) and have both a phase shift of $\pm \pi/2$ with respect to \tilde{h}_2^l [31, 32, 58], the total impact of \tilde{h}_1^l on the excitation of the optical SW modes is low. In the FM and AFM configuration, the total impact of \tilde{h}_1^l on the magnetization precession almost cancels because the top Co(4) layer is thicker but has a lower magnitude $\tilde{h}_1^B \propto b_2^B \tilde{a}_{xz} = i0.22$ T than the bottom Co(2) layer. Identical simulations of $\Delta S_{ij}(\mu_0H, \phi_H)$ but with

$b_2^B \tilde{a}_{xz} \gg i0.22$ T or $b_2^B \tilde{a}_{xz} \ll i0.22$ T show a nonreciprocal excitation efficiency because of the SAW-SW helicity mismatch effect, as demonstrated in Appendix E. For the investigated sample, the impact of the SAW-SW helicity mismatch effect on the nonreciprocal transmission is rather small.

V. CONCLUSIONS

In conclusion, we have experimentally studied the SAW-SW interaction in SAFs. Our experiments are in good agreement with analytical model calculations, including interlayer exchange coupling, iDMI, and IDC. The model describes the experimental findings of the studied Pt/Co(2)/Ru/Co(4)/Pt SAF for multiple frequencies and different external magnetic field magnitudes, which can be used to switch the equilibrium magnetization directions in both Co layers from AFM to C to FM configuration. While the magnetoacoustic excitation efficiency of SWs is maximized in the AFM configuration, it is medium in the C configuration and low in the FM configuration. This is a consequence of the excited optical SW mode in the SAF and the directions and magnitudes of the magnetoacoustic driving fields in both Co layers. Efficient SAW-driven SW excitation should be even possible in compensated SAFs with zero net magnetization. This is in contrast to the small excitation efficiency of the optical SW mode by Oersted fields employing antennas [35].

Moreover, we demonstrate a large nonreciprocity Δf_{\pm} of the SW dispersion because of the individual additive nonreciprocal contributions of iDMI and IDC. In the Damon-Eshbach geometry ($\phi_0^l = \pm 90^\circ$) and AFM configuration, both contributions give rise to $\Delta f_{\pm} \approx 3$ GHz for SWs with $f = 6.77$ GHz and $k = 13.1 \mu\text{m}^{-1}$. The nonreciprocity Δf_{\pm} switches the sign and is much lower

in the FM configuration. The strength of the interlayer exchange interaction has a strong impact on the static magnetization configuration, which in turn governs the SW resonance frequency $f(\mu_0 H)$ and nonreciprocity Δf_{\pm} by iDMI and IDC. This explains the dependence of the magnetoacoustic response ΔS_{ij} on the nonmagnetic spacer layer thickness d_s , as experimentally observed in Ref. [33]. Because of the high SW damping α and the low magnetic film thicknesses used, the maximum nonreciprocity of the SAW transmission $\Delta S_{\pm} \approx 2$ dB is moderate in comparison to magnetic bilayers and SAFs with low-damping and thicker ferromagnetic layers ($\Delta S_{\pm} \approx 30$ dB) [29, 30, 33].

ACKNOWLEDGMENTS

This work is funded by the Deutsche Forschungsgemeinschaft (DFG, German Research Foundation) – project number 492421737.

Appendix A: Equilibrium state of the magnetization

The equilibrium magnetization direction ϕ_0^l is calculated by numerical minimization of the static free energy E_S per surface area [23, 37] in the xyz coordinate system

$$E_S = \sum_{l=A,B} d^l M_s^l \left(-\mu_0 \mathbf{H} \cdot \mathbf{m}^l + \frac{1}{2} \mu_0 (M_s^l - H_k^l) (m_z^l)^2 - \frac{1}{2} \mu_0 H_{\text{ani}}^l (\mathbf{m}^l \cdot \mathbf{u}^l)^2 \right) - J_{\text{eff}} \mathbf{m}^A \cdot \mathbf{m}^B, \quad (\text{A1})$$

where $\mathbf{m}^l = \mathbf{M}^l / M_s^l$ are the unit vectors of the magnetizations \mathbf{M}^l . We consider the Zeeman energy, demagnetization field, which is partly compensated by a surface anisotropy field H_k , an in-plane uniaxial anisotropy field $\mu_0 H_{\text{ani}}$ with the easy-axis direction along \mathbf{u} and bilinear interlayer exchange coupling. The unit vector \mathbf{u} is assumed to be orientated in the plane of the magnetic film and makes the angle ϕ_{ani}^l with the x axis. We neglect interlayer demagnetization fields since the lateral size of the fabricated sample is much larger than its thickness [23, 59].

Appendix B: Effective dipolar fields

The effective fields caused by iDMI are taken from Moon et al. [14]

$$\mathbf{H}_{\text{eff},123,\text{DMI}}^l = i \frac{2D_{\text{eff}}^l}{\mu_0 M_s^l} k \sin(\phi_0^l) \begin{pmatrix} -m_2^l \\ m_1^l \end{pmatrix}. \quad (\text{B1})$$

Moreover, the effective fields of the bilinear interlayer exchange coupling

$$\mathbf{H}_{\text{eff},123,\text{IEC}}^A = \frac{J_{\text{bl}}}{d^A \mu_0 M_s^A} \begin{pmatrix} m_1^B \\ \cos(\phi_0^A - \phi_0^B) m_2^B \\ \cos(\phi_0^A - \phi_0^B) \end{pmatrix} \quad (\text{B2})$$

and interlayer dipolar fields

$$\mathbf{H}_{\text{eff},123,\text{IDC}}^A = -M_s^B G_0^A G_0^B \frac{d^B}{2} e^{-|k|d_s} \times \begin{pmatrix} -|k| m_1^B - i \sin(\phi_0^B) k m_2^B \\ \sin(\phi_0^A) \sin(\phi_0^B) |k| m_2^B - i \sin(\phi_0^A) k m_1^B \\ 0 \end{pmatrix}, \quad (\text{B3})$$

are taken from Gallardo et al. [12] and rewritten in the $(\mathbf{e}_1^l, \mathbf{e}_2^l, \mathbf{e}_3^l)$ -coordinate system. Hereby, $G_0^l = (1 - e^{-|k|d^l}) / (|k|d^l)$ are dipolar SW terms [60]. For the effective fields $\mathbf{H}_{\text{eff},123,\text{IEC}}^B$ and $\mathbf{H}_{\text{eff},123,\text{IDC}}^B$ of layer B , the replacements $A \rightarrow B$, $B \rightarrow A$, and $-i \rightarrow +i$ are carried out.

Appendix C: Sample preparation

After preparation of the IDTs, rectangular-shaped Pt(3)/Co(2)/Ru(0.85)/Co(4)/Pt(3)/Si₃N₄(3) SAFs (thicknesses are given in nm) were deposited at room temperature by magnetron sputtering (base pressure $< 1 \times 10^{-8}$ mbar) between the IDTs. The Ar pressure was kept constant at 3.5×10^{-3} mbar during the deposition process and the sample holder was rotating during sputtering. The individual layer thicknesses were determined using a calibrated deposition rate (Pt: 0.05 nm/s, Co: 0.02 nm/s, Ru: 0.025 nm/s and Si₃N₄: 0.0065 nm/s). The Si₃N₄(3) capping layer prevents oxidation of the SAF.

Appendix D: Simulation parameters

In this section, we describe how the simulation parameters in Table I were derived. First, we determined the effective interlayer coupling constant J_{eff} from the M - H hysteresis loop in Fig. 2(a). We used the macrospin model to simulate M - H . With the saturation magnetizations M_s^l obtained by SQUID-VSM measurements performed on single layer reference samples and the nominal magnetic thin film thicknesses d^l , we obtain rather good agreement between experiment and simulation for $J_{\text{eff}} = -0.95$ mJ/m². This value is in the same range as reported in the literature for similar SAFs [34, 37]. Discrepancies between experiment and simulation are attributed to the simplification of the macrospin approach [61]. In agreement with the literature, biquadratic interlayer exchange coupling [12, 36, 62] is usually neglected to describe the magnetic behavior of Co/Ru/Co multilayers [27, 34, 37, 50, 63].

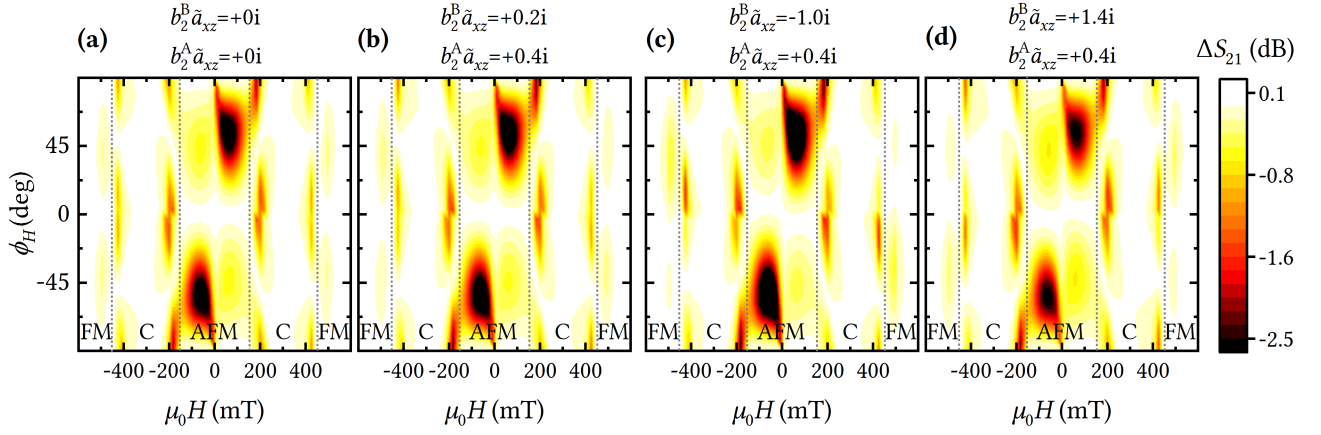


FIG. 7. The out-of-plane magnetoacoustic driving field $\tilde{h}_1^l \propto b_2^l \tilde{a}_{xz}$ is changed in simulations to probe the impact of the SAW-SW helicity mismatch effect on the SAW transmission $\Delta S_{ij}(\mu_0 H, \phi_H)$ at 6.77 GHz. (a) The SAW-SW helicity mismatch effect vanishes for an in-plane linear polarized driving field. The results in (a) are almost identical to the results in (b), for which the same simulation parameters as in all previous simulations were used. Thus, the impact of the SAW-SW helicity mismatch effect is small in the simulations in Figs. 5 and 6. If the driving field $\tilde{h}_1^B \propto b_2^B \tilde{a}_{xz}$ of the top Co layer is artificially low (c) or high (d), the SAW-SW helicity mismatch effect modulates slightly the SAW transmission nonreciprocity.

Furthermore, for the simulations, we use M_s^l , the g -factor, H_k^l , and α^l obtained by SQUID-VSM and bbFMR measurements performed on the single layer reference samples. These parameters are summarized in Table I. Hereby, the Gilbert damping α_{FMR}^l and the inhomogeneous line broadening ΔH_{FMR}^l contribute to the effective SW damping constant [31]

$$\alpha^l = \frac{\gamma^l}{2\omega} \mu_0 \Delta H_{\text{FMR}}^l + \alpha_{\text{FMR}}^l, \quad (\text{D1})$$

where γ^l is the absolute value of the gyromagnetic ratio. The magnetic exchange constant $A_{\text{ex}}^l = 31$ pJ/m is taken from the literature [23, 56]. In addition, D_{eff}^A and $b_1^A \tilde{a}_{xx}$ are taken from magnetoacoustic transmission measurements, which were performed on a LiNbO₃/Pt(3)/Co(2)/Ru(0.85)/Si₃N₄(3) sample and carried out as described in Ref. [31]. Because of the interface character of iDMI and $d^A = 0.5d^B$, we assume that $D_{\text{eff}}^B = 0.5D_{\text{eff}}^A$.

Finally, we use Eq. (6) to simulate the experimental results of the SAF as presented in Figs. 5 and 6. Experiment and simulation show good quantitative agreement under the assumptions for $b_1^B \tilde{a}_{xx}$, $b_2^B \tilde{a}_{xz}$, and the uniaxial anisotropies, given in Table I. Since the uniaxial anisotropies are small ($\mu_0 H_{\text{ani}}^l \leq 4$ mT) in comparison to the external magnetic field magnitude ($|\mu_0 H| \leq 600$ mT), the anisotropies have mainly an impact around zero field. We attribute different magnetoelastic constants $b_{1,2}^A$ and $b_{1,2}^B$ of the bottom and top Co layer to different growth conditions caused by different seed layers and thicknesses.

Appendix E: Impact of the helicity mismatch effect

The nonreciprocal SAW transmission in magnetoacoustic transmission measurements can be also caused by the nonreciprocity of the SW dispersion and/or the SAW-SW helicity mismatch effect. By changing the helicity of the magnetoacoustic driving field in the simulations, we additionally study the impact of the SAW-SW helicity mismatch effect on the SAW transmission. In Fig. 7, we show the simulated SAW transmission $\Delta S_{21}(\mu_0 H, \phi_H)$ with the parameters of Table I, but with modified values for the out-of-plane magnetoacoustic driving field $\tilde{h}_1^l \propto b_2^l \tilde{a}_{xz}$ [see Eq. (4)]. The SAW-SW helicity mismatch effect vanishes for $b_2^A \tilde{a}_{xz} = b_2^B \tilde{a}_{xz} = 0i$ in Fig. 7(a), because the driving field is in-plane linear polarized. The results in Fig. 7(a) are almost identical to the results in Fig. 7(b), for which the same simulation parameters as in all previous simulations were used. Thus, the impact of the SAW-SW helicity mismatch effect on the nonreciprocal transmission in the previous simulations is very small.

If the driving field [\tilde{h}_1^B] of the top Co layer is artificially large, the SAW-SW helicity mismatch effect modulates the SAW transmission nonreciprocity. For instance, with an increase of $b_2^B \tilde{a}_{xz}$ in Figs. 7(c), 7(b), and 7(d) the SAW absorption of the SAW-SW resonance in the AFM configuration increases in the 2nd quadrant and decreases in the 3rd quadrant. Additionally, the intensity of the resonances in the FM configuration differs between the 2nd and 3rd quadrant for the artificially large $|b_2^B \tilde{a}_{xz}|$ in Figs. 7(c) and 7(d). Such an asymmetry of the intensity of the resonances in the FM configuration is not observed in the experimental results presented in Fig. 5(a). We conclude that the impact of the SAW-SW helicity mismatch effect on the nonreciprocal transmission of the investigated sample is rather small in comparison to the impact of the nonreciprocity of the SW dispersion.

- [1] R. M. White and F. W. Voltmer, Direct piezoelectric coupling to surface elastic waves, *Appl. Phys. Lett.* **7**, 314 (1965).
- [2] C. K. Campbell, *Surface acoustic wave devices for mobile and wireless communications* (Academic Press, San Diego, CA, 1998).
- [3] D. P. Morgan, *Surface Acoustic Wave Filters: With Applications to Electronic Communications and Signal Processing*, 2nd ed. (Elsevier, Amsterdam, 2007).
- [4] Z. Guttenberg, H. Müller, H. Habermüller, A. Geisbauer, J. Pipper, J. Felbel, M. Kielpinski, J. Scriba, and A. Wixforth, Planar chip device for PCR and hybridization with surface acoustic wave pump, *Lab Chip* **5**, 308 (2005).
- [5] X. Ding, P. Li, S.-C. S. Lin, Z. S. Stratton, N. Nama, F. Guo, D. Slotcavage, X. Mao, J. Shi, F. Costanzo, and T. J. Huang, Surface acoustic wave microfluidics, *Lab Chip* **13**, 3626 (2013).
- [6] A. Wixforth, J. P. Kotthaus, and G. Weimann, Quantum oscillations in the surface-acoustic-wave attenuation caused by a two-dimensional electron system, *Phys. Rev. Lett.* **56**, 2104 (1986).
- [7] C. H. W. Barnes, J. M. Shilton, and A. M. Robinson, Quantum computation using electrons trapped by surface acoustic waves, *Phys. Rev. B: Condens. Matter* **62**, 8410 (2000).
- [8] B. Paschke, A. Wixforth, D. Denysenko, and D. Volkmer, Fast surface acoustic wave-based sensors to investigate the kinetics of gas uptake in ultra-microporous frameworks, *ACS Sens.* **2**, 740 (2017).
- [9] K. Länge, B. E. Rapp, and M. Rapp, Surface acoustic wave biosensors: a review, *Anal. Bioanal. Chem.* **391**, 1509 (2008).
- [10] S. G. Joshi, Flow sensors based on surface acoustic waves, *Sens. Actuators A: Phys.* **44**, 191 (1994).
- [11] A. Barman, G. Gubbiotti, S. Ladak, A. O. Adeyeye, M. Krawczyk, J. Gräfe, C. Adelman, S. Coto-fana, A. Naeemi, V. I. Vasyuchka, B. Hillebrands, S. A. Nikitov, H. Yu, D. Grundler, A. V. Sadovnikov, A. A. Grachev, S. E. Sheshukova, J.-Y. Duquesne, M. Marangolo, G. Csaba, W. Porod, V. E. Demidov, S. Urazhdin, S. O. Demokritov, E. Albisetti, D. Petti, R. Bertacco, H. Schultheiss, V. V. Kruglyak, V. D. Poimanov, S. Sahoo, J. Sinha, H. Yang, M. Münzenberg, T. Moriyama, S. Mizukami, P. Landeros, R. A. Gallardo, G. Carlotti, J.-V. Kim, R. L. Stamps, R. E. Camley, B. Rana, Y. Otani, W. Yu, T. Yu, G. E. W. Bauer, C. Back, G. S. Uhrig, O. V. Dobrovolskiy, B. Budinska, H. Qin, S. van Dijken, A. V. Chumak, A. Khitun, D. E. Nikonov, I. A. Young, B. W. Zingsem, and M. Winklhofer, The 2021 magnonics roadmap, *J. Phys.: Condens. Matter* **33**, 413001 (2021).
- [12] R.A. Gallardo, T. Schneider, A.K. Chaurasiya, A. Oelschlägel, S.S.P.K. Arekapudi, A. Roldán-Molina, R. Hübner, K. Lenz, A. Barman, J. Fassbender, J. Lindner, O. Hellwig, and P. Landeros, Reconfigurable spin-wave nonreciprocity induced by dipolar interaction in a coupled ferromagnetic bilayer, *Phys. Rev. Applied* **12**, 034012 (2019).
- [13] M. Ishibashi, Y. Shiota, T. Li, S. Funada, T. Moriyama, and T. Ono, Switchable giant nonreciprocal frequency shift of propagating spin waves in synthetic antiferromagnets, *Sci. Adv.* **6**, eaaz6931 (2020).
- [14] J.-H. Moon, S.-M. Seo, K.-J. Lee, K.-W. Kim, J. Ryu, H.-W. Lee, R. D. McMichael, and M. D. Stiles, Spin-wave propagation in the presence of interfacial Dzyaloshinskii-Moriya interaction, *Phys. Rev. B* **88**, 184404 (2013).
- [15] D. Cortés-Ortuño and P. Landeros, Influence of the Dzyaloshinskii-Moriya interaction on the spin-wave spectra of thin films, *J. Phys.: Condens. Matter* **25**, 156001 (2013).
- [16] H. T. Nembach, J. M. Shaw, M. Weiler, E. Jué, and T. J. Silva, Linear relation between Heisenberg exchange and interfacial Dzyaloshinskii-Moriya interaction in metal films, *Nat. Phys.* **11**, 825 (2015).
- [17] K. Di, V. L. Zhang, H. S. Lim, S. C. Ng, M. H. Kuok, J. Yu, J. Yoon, X. Qiu, and H. Yang, Direct observation of the Dzyaloshinskii-Moriya interaction in a Pt/Co/Ni film, *Phys. Rev. Lett.* **114**, 047201 (2015).
- [18] M. Belmeguenai, J.-P. Adam, Y. Roussigné, S. Eimer, T. Devolder, J.-V. Kim, S. M. Cherif, A. Stashkevich, and A. Thiaville, Interfacial Dzyaloshinskii-Moriya interaction in perpendicularly magnetized Pt/Co/AlO_x ultrathin films measured by Brillouin light spectroscopy, *Phys. Rev. B* **91**, 180405(R) (2015).
- [19] R. E. Camley and A. A. Maradudin, Magnetostatic interface waves in ferromagnets, *Solid State Commun.* **41**, 585 (1982).
- [20] P. Grünberg, Some ways to modify the spin-wave mode spectra of magnetic multilayers, *J. Appl. Phys.* **57**, 3673 (1985).
- [21] P. Bruno and C. Chappert, Oscillatory coupling between ferromagnetic layers separated by a nonmagnetic metal spacer, *Phys. Rev. Lett.* **67**, 1602 (1991).
- [22] R. A. Duine, Kyung-Jin Lee, Stuart S. P. Parkin, and M. D. Stiles, Synthetic antiferromagnetic spintronics, *Nat. Phys.* **14**, 217 (2018).
- [23] A. F. Franco and P. Landeros, Enhancement of the spin-wave nonreciprocity in antiferromagnetically coupled multilayers with dipolar and interfacial Dzyaloshinskii-Moriya interactions, *Phys. Rev. B* **102**, 184424 (2020).
- [24] M. Küß, M. Albrecht, and M. Weiler, Chiral magnetoacoustics, *Front. Phys.* **10**, 981257 (2022).
- [25] W.-G. Yang and H. Schmidt, Acoustic control of magnetism toward energy-efficient applications, *Appl. Phys. Rev.* **8**, 021304 (2021).
- [26] R. Verba, I. Lisenkov, I. Krivorotov, V. Tiberkevich, and A. Slavin, Nonreciprocal surface acoustic waves in multilayers with magnetoelastic and interfacial Dzyaloshinskii-Moriya interactions, *Phys. Rev. Applied* **9**, 064014 (2018).
- [27] R. Verba, V. Tiberkevich, and A. Slavin, Wide-band nonreciprocity of surface acoustic waves induced by magnetoelastic coupling with a synthetic antiferromagnet, *Phys. Rev. Applied* **12**, 054061 (2019).
- [28] R. Verba, E. N. Bankowski, T. J. Meitzler, V. Tiberkevich, and A. Slavin, Phase nonreciprocity of microwave-frequency surface acoustic waves in hybrid heterostructures with magnetoelastic coupling, *Adv. Electron. Mater.* **7**, 2100263 (2021).
- [29] P. J. Shah, D. A. Bas, I. Lisenkov, A. Matyushov, N. X. Sun, and M. R. Page, Giant nonreciprocity of surface acoustic waves enabled by the magnetoelastic interaction,

- Sci. Adv. **6**, eabc5648 (2020).
- [30] M. Küß, M. Heigl, L. Flacke, A. Hörner, M. Weiler, A. Wixforth, and M. Albrecht, Nonreciprocal magnetoacoustic waves in dipolar-coupled ferromagnetic bilayers, *Phys. Rev. Applied* **15**, 034060 (2021).
- [31] M. Küß, M. Heigl, L. Flacke, A. Hörner, M. Weiler, M. Albrecht, and A. Wixforth, Nonreciprocal Dzyaloshinskii–Moriya magnetoacoustic waves, *Phys. Rev. Lett.* **125**, 217203 (2020).
- [32] M. Xu, K. Yamamoto, J. Puebla, K. Baumgaertl, B. Rana, K. Miura, H. Takahashi, D. Grundler, S. Maekawa, and Y. Otani, Nonreciprocal surface acoustic wave propagation via magneto-rotation coupling, *Sci. Adv.* **6**, eabb1724 (2020).
- [33] H. Matsumoto, T. Kawada, M. Ishibashi, M. Kawaguchi, and M. Hayashi, Large surface acoustic wave nonreciprocity in synthetic antiferromagnets, *Appl. Phys. Express* **15**, 063003 (2022).
- [34] P. J. H. Bloemen, H. W. van Kesteren, H. J. M. Swagten, and W. J. M. de Jonge, Oscillatory interlayer exchange coupling in Co/Ru multilayers and bilayers, *Phys. Rev. B: Condens. Matter* **50**, 13505 (1994).
- [35] Z. Zhang, L. Zhou, P. E. Wigen, and K. Ounadjela, Angular dependence of ferromagnetic resonance in exchange-coupled Co/Ru/Co trilayer structures, *Phys. Rev. B* **50**, 6094 (1994).
- [36] S. O. Demokritov, Biquadratic interlayer coupling in layered magnetic systems, *J. Phys. D* **31**, 925 (1998).
- [37] G. J. Strijkers, S. M. Zhou, F. Y. Yang, and C. L. Chien, Magnetic characterization and modeling of FeMn/Co/Ru/Co artificial antiferromagnets, *Phys. Rev. B* **62**, 13896 (2000).
- [38] B. Heinrich, Y. Tserkovnyak, G. Woltersdorf, A. Brataas, R. Urban, and G. E. W. Bauer, Dynamic exchange coupling in magnetic bilayers, *Phys. Rev. Lett.* **90**, 187601 (2003).
- [39] S. Sorokin, R. A. Gallardo, C. Fowley, K. Lenz, A. Titova, G. Y. P. Atcheson, G. Dennehy, K. Rode, J. Fassbender, J. Lindner, and A. M. Deac, Magnetization dynamics in synthetic antiferromagnets: Role of dynamical energy and mutual spin pumping, *Phys. Rev. B* **101**, 144410 (2020).
- [40] W. P. Robbins, A simple method of approximating surface acoustic wave power densities, *IEEE Trans. Son. Ultrason.* **24**, 339 (1977).
- [41] L. Dreher, M. Weiler, M. Pernpeintner, H. Huebl, R. Gross, M. S. Brandt, and S. T. B. Goennenwein, Surface acoustic wave driven ferromagnetic resonance in nickel thin films: Theory and experiment, *Phys. Rev. B* **86**, 134415 (2012).
- [42] C. Kittel, Interaction of spin waves and ultrasonic waves in ferromagnetic crystals, *Phys. Rev.* **110**, 836 (1958).
- [43] S. Maekawa and M. Tachiki, Surface acoustic attenuation due to surface spin wave in ferro- and antiferromagnets, *AIP Conf. Proc.* **29**, 542 (1976).
- [44] M. Matsuo, J. Ieda, E. Saitoh, and S. Maekawa, Effects of mechanical rotation on spin currents, *Phys. Rev. Lett.* **106**, 076601 (2011).
- [45] M. Matsuo, J. Ieda, K. Harii, E. Saitoh, and S. Maekawa, Mechanical generation of spin current by spin-rotation coupling, *Phys. Rev. B* **87**, 180402(R) (2013).
- [46] D. Kobayashi, T. Yoshikawa, M. Matsuo, R. Iguchi, S. Maekawa, E. Saitoh, and Y. Nozaki, Spin current generation using a surface acoustic wave generated via spin-rotation coupling, *Phys. Rev. Lett.* **119**, 077202 (2017).
- [47] Y. Kurimune, M. Matsuo, and Y. Nozaki, Observation of gyromagnetic spin wave resonance in NiFe films, *Phys. Rev. Lett.* **124**, 217205 (2020).
- [48] M. Weiler, L. Dreher, C. Heeg, H. Huebl, R. Gross, M. S. Brandt, and S. T. B. Goennenwein, Elastically driven ferromagnetic resonance in nickel thin films, *Phys. Rev. Lett.* **106**, 117601 (2011).
- [49] K. Ounadjela, A. Arbaoui, A. Herr, R. Poinsoot, A. Dinia, D. Muller, and P. Panissod, Interlayer exchange coupling in Co/Ru superlattices, *J. Magn. Magn. Mater.* **106**, 1896 (1992).
- [50] Parkin, More, and Roche, Oscillations in exchange coupling and magnetoresistance in metallic superlattice structures: Co/Ru, Co/Cr, and Fe/Cr, *Phys. Rev. Lett.* **64**, 2304 (1990).
- [51] H. Yang, A. Thiaville, S. Rohart, A. Fert, and M. Chshiev, Anatomy of Dzyaloshinskii–Moriya interaction at Co/Pt interfaces, *Phys. Rev. Lett.* **115**, 267210 (2015).
- [52] J. Cho, N.-H. Kim, S. Lee, J.-S. Kim, R. Lavrijsen, A. Solignac, Y. Yin, D.-S. Han, van Hoof, Niels J. J., H. J. M. Swagten, B. Koopmans, and C.-Y. You, Thickness dependence of the interfacial Dzyaloshinskii–Moriya interaction in inversion symmetry broken systems, *Nat. Commun.* **6**, 7635 (2015).
- [53] M. Hiebel, *Grundlagen der vektoriellen Netzwerkanalyse*, 3rd ed. (Rohde & Schwarz, München, 2011).
- [54] P. G. Gowtham, T. Moriyama, D. C. Ralph, and R. A. Buhrman, Traveling surface spin-wave resonance spectroscopy using surface acoustic waves, *J. Appl. Phys.* **118**, 233910 (2015).
- [55] The propagation velocity of a Rayleigh-type SAW on a pure Y-cut Z-propagation LiNbO₃ substrate with a perfectly conducting overlayer of zero thickness is $c_{SAW} = 3404 \text{ m/s}$ [3]. We assume that c_{SAW} in the real piezoelectric-ferromagnetic heterostructure is slightly lowered [30] because of mass loading and different elastic constants of LiNbO₃ and the magnetic films.
- [56] G. Bertotti, *Hysteresis in Magnetism: For Physicists, Materials Scientists, and Engineers*, Electromagnetism (Academic Press, New York, 1998).
- [57] Y. Tserkovnyak, A. Brataas, and G. E. W. Bauer, Enhanced Gilbert damping in thin ferromagnetic films, *Phys. Rev. Lett.* **88**, 117601 (2002).
- [58] R. Sasaki, Y. Nii, Y. Iguchi, and Y. Onose, Nonreciprocal propagation of surface acoustic wave in Ni/LiNbO₃, *Phys. Rev. B* **95**, 020407(R) (2017).
- [59] A. F. Franco, Intensity enhancement of ferromagnetic resonance modes in exchange coupled magnetic multilayers, *New J. Phys.* **22**, 013017 (2020).
- [60] B. A. Kalinikos and A. N. Slavin, Theory of dipole-exchange spin wave spectrum for ferromagnetic films with mixed exchange boundary conditions, *J. Phys. C* **19**, 7013 (1986).
- [61] C. Tannous and J. Gieraltowski, The Stoner–Wohlfarth model of ferromagnetism, *Eur. J. Phys.* **29**, 475 (2008).
- [62] S. M. Rezende, C. Chesman, M. A. Lucena, A. Azevedo, F. M. de Aguiar, and S. S. P. Parkin, Studies of coupled metallic magnetic thin-film trilayers, *J. Appl. Phys.* **84**, 958 (1998).
- [63] A. G. Kolesnikov, V. S. Plotnikov, E. V. Pustovalov, A. S. Samardak, L. A. Chebotkevich, A. V. Ognev, and O. A. Tretiakov, Composite topological structure of do-

main walls in synthetic antiferromagnets, *Sci. Rep.* **8**,
15794 (2018).